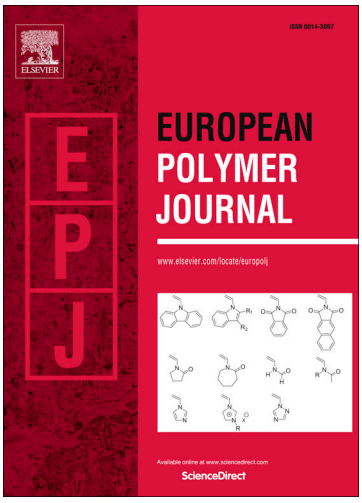

Thermally-triggered free-standing shape-memory actuators

Alberto Belmonte, Giuseppe C. Lama, Gennaro Gentile, Pierfrancesco Cerruti, Veronica Ambrogi, Xavier Fernández-Francos, Silvia De la Flor

PII: S0014-3057(17)31324-1
DOI: https://doi.org/10.1016/j.eurpolymj.2017.10.006
Reference: EPJ 8105

To appear in: *European Polymer Journal*

Received Date: 25 July 2017
Revised Date: 5 October 2017
Accepted Date: 7 October 2017

Please cite this article as: Belmonte, A., Lama, G.C., Gentile, G., Cerruti, P., Ambrogi, V., Fernández-Francos, X., De la Flor, S., Thermally-triggered free-standing shape-memory actuators, *European Polymer Journal* (2017), doi: https://doi.org/10.1016/j.eurpolymj.2017.10.006

Thermally-triggered free-standing shape-memory actuators

Alberto Belmonte[1], Giuseppe C. Lama[2,3], Gennaro Gentile[3], Pierfrancesco Cerruti[3], Veronica Ambrogi[2,3], Xavier Fernández-Francos[4], Silvia De la Flor[1]*.

[1] Department of Mechanical Engineering, Universitat Rovira i Virgili, Av. Països Catalans, 26, 43007, Tarragona (Spain), albertofrancisco.belmonte@urv.cat

[2] Department of Chemical, Materials and Production Engineering, University of Naples "Federico II", Piazzale Tecchio, 80, 80125, Napoli (Italy), giuseppecesare.lama@live.it and ambrogi@unina.it

[3] Institute for Polymers, Composites and Biomaterials, National Council of Research of Italy, Via Campi Flegrei, 34, 80078, Pozzuoli (NA) (Italy), cerruti@ipcb.cnr.it and gennaro.gentile@ipcb.cnr.it

[4] Thermodynamics Laboratory ETSEIB, Universitat Politècnica de Catalunya, Av. Diagonal, 647, 08028, Barcelona (Spain), xavier.fernandez@mmt.upc.edu

* Correspondence: silvia.delaflor@urv.cat; Tel.: +34-977558839; Fax: +34-977559602

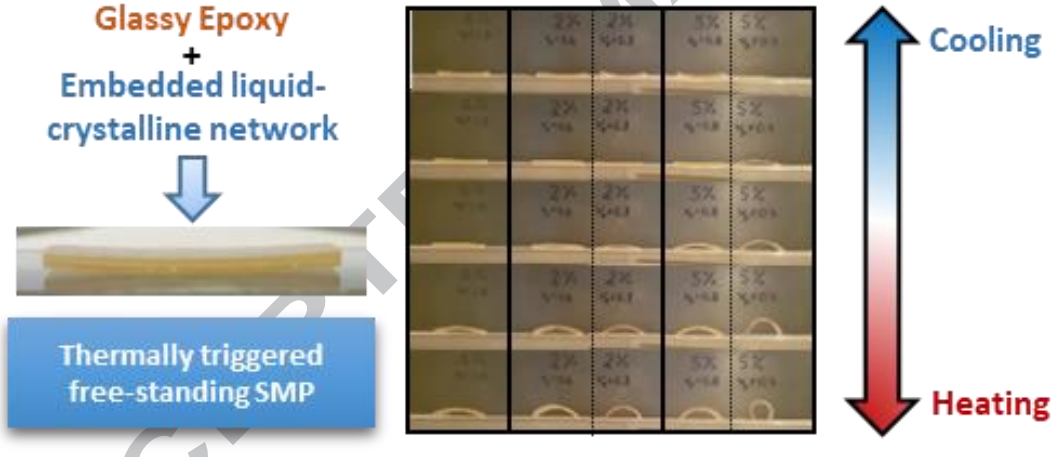

Highlights

1. Free-standing stimuli-triggered two-way shape memory polymer is designed by joining together a programmed liquid-crystalline network film and a glassy thermoset.
2. Reversible bending actuation motion is achieved by assembling beam-like multilayered devices using layers of both materials with the same surface.
3. Modulating the actuation level is possible by adjusting the thickness of the different layers and the stretching level of the liquid-crystalline network (device configuration).
4. An analytical model based on multilayered devices makes possible to predict the actuation level depending on the materials properties and configuration.

ABSTRACT

This investigation presents a new approach to obtain free-standing thermally-triggered "two-way" shape-memory actuators by realizing multilayer structures constituted by glassy thermoset (GT) films anchored to a previously programmed liquid-crystalline network (LCN) film. The GT is obtained via dual-curing of off-stoichiometric "thiol-epoxy" mixtures, thus enabling the development of complex actuator configurations thanks to the easy processing in the intermediate stage, and a compact and resistant design due to the strong adhesion between the layers obtained upon the final curing stage of the GT. A model based on the classical multilayered beam theory to predict the maximum deflection of a "beam-like" design is proposed and its reliability is verified by experimental investigation of actuators with different configurations and LCN stretching levels. The results show the capability of these actuators to bend and unbend under various consecutive heating-cooling procedures in a controlled way. The maximum deflection can be modulated through the configuration and the LCN stretching level, showing an excellent fitting with the model predictions. The model is able to predict high actuation levels (angles of curvature ≈ 180^{o}) and the bidirectional shape-memory behavior of the device as a function of the thickness, configuration of the layers, and the LCN stretching level. This approach enables the design of free-standing two-way actuators covering a range of bending actuation from 27 to 98% of the theoretical maximum deflection.

KEYWORDS. Shape memory polymers, thermally-triggered actuators, click chemistry, dual-curing, liquid-crystalline network

1. INTRODUCTION

Shape-memory polymers (SMPs) are a class of responsive materials capable to shift under an external stimulus from one temporary shape to the original shape, usually fixed during the curing process[1–3]. The shape-transformation, commonly referred to shape-memory effect (SME), is not an intrinsic property of the polymer, but a consequence of an external treatment (programming process). The material must undergo a transformation from a stable state of the network (original shape) to one or more unstable states (temporary shapes) usually through thermomechanical procedures. These temporary shapes are stabilized by the formation of strong interactions within the network that impede the recovery of the original shape until an external stimulus, such as heat, is applied[4,5]. During this process, the material stores an amount of energy that is then released in form of shape-transformation or force[6–10]. This makes this class of materials attractive in many fields of applications, such as industrial applications (i.e. opening-closing mechanisms[11]), aviation (i.e. morphing structures[12]) and robotics (i.e. artificial muscles[13]).

Liquid-crystalline networks (LCN) are a class of SMPs capable of shifting from one to another temporary shape (two-way SMPs) in a reversible way under the effect of a constant load and an external stimulus, thus, only an initial programming process is required[14,15]. The reversible transformation is caused by the formation and alignment of liquid-crystalline (LC) domains in the load direction (induced-

elongation) and further disordering of the LC domains (shrinkage) during the LC transition[16,17]. LCNs are potential candidates for actuation purposes due to their shape-shifting capability[18–20], but the need of a constant load in the shifting direction limits considerably their application. Recently, some strategies to overcome this limitation have been proposed. All of them depend on the incorporation of an internal or external stress-applying component into an already stretched LCN network (microscopic[21,22] or macroscopic[23,24] composites respectively), hindering the recovery of the original shape, but adopting a metastable shape "state-of-ease" after the LCN shrinkage. This state can help to further elongate back to the original shape thanks to the internal stress generated between both the stress-applying component and the LCN[25,26]. In general words, combining a stress-applying component with a shape-shifting component leads to free-standing reversible actuation when compatibility between them is attained. The external incorporation of the stress-applying component was first reported by Westbrook et al.[27,28], who embedded a stretched poly(cyclooctene)-based LCN into an elastomeric matrix through thermal curing of the latter. The resulting material was able to produce small reversible flexural actuation by heating-cooling procedures. The internal approach could be achieved by taking advantage of two-stage curing procedures[22,29,30]. Anthamatten et al.[22] cured partially-crosslinked semicrystalline poly(ε-caprolactone) networks after the 1st curing stage, stretched them up to 650% of strain and fixed the shape by UV-crosslinking (2nd curing stage). However, the actuation strain was lower than 15%. Yakacki et al.[29,30], enhanced the actuation strain up to 110% (with a programmed strain of 400%) by using a "thiol-acrylate" two-stage curing procedure with crosslinks of different functionality. Other approaches consisting of semi crystalline networks with two crystalline domains or confined crystalline domains have been reported[31].

To this end, novel strategies to develop free-standing "two-way" SMPs are necessary to fulfill the increasing demand of smart actuators. Nowadays, their actuation response is limited to common designs and their performance is too low in comparison with common "two-way" SMPs. In this work, a new methodology to develop free-standing "two-way" SMPs with an enhanced control of the actuation response is presented. An epoxy-based glassy thermoset (GT) obtained via sequential dual-curing of stoichiometrically imbalanced "thiol-epoxy" mixtures is used as external stress-applying component[32]. An epoxy-based lightly crosslinked LCN with high isotropization temperature (T_{iso}) is used as shape-shifting component[33]. The assembly of actuators with different configuration and actuation response is attained thanks to the possibility of pre-designing the GT component in the shape of solid-like and sticky layers with controllable thickness after the 1st curing stage that are further attached to the stretched LCN (shape-shifting component) through the 2nd curing stage of the former (multilayer assembling methodology)[34]. The actuator response depends on the capability of the LCN to deform the device during the shrinkage (heating above T_{iso}) and the capability of the GT to stress back the LCN during the induced-elongation (cooling below T_{iso}). This can be achieved thanks to the rubbery elastic mechanical response of the GT material above T_g[35]. If the T_g of the GT is lower than T_{iso}, and operation of the GT-LCN assembly takes place only above this T_g, the GT will be in the rubbery state during both cooling and shrinkage processes, thus, making possible the elastic response. The way in which the actuator works is defined by the thermo-mechanical properties of the materials, the stretching level of the LCN, the adhesion between layers and the assembled configuration. In the present work, all this parameters are investigated and an analytical model to predict the actuation response is proposed.

Experimental analyses are carried out with different actuator configurations and LCN stretching levels and the results are compared with the model predictions.

2. EXPERIMENTAL SECTION

2.1 Materials

2.1.1. Actuator shape-shifting component: epoxy-based LCN

A commercial diol (4,4'-dihydroxybiphenyl, DIF, 97% purity, 186.21 g/mol), epichlorohydrin (Sigma-Aldrich, 99% purity, 1.183 g/ml, 92.52 g/mol), isopropanol and sodium hydroxide were used for the preparation of the epoxy-based mesogenic compound by epoxidation of the DIF monomer[36]. A commercial acid (1,8-octanedicarboxylic acid, sebacic acid, 98% purity, 202.25 g/mol) was used as curing agent of the mesogenic compound for the synthesis of the LCN. Trycaprylyl methylammonium chloride was used as catalyst of the reaction. As it was reported[33], the use of sebacic acid as curing agent of this epoxy-based mesogen leads to the formation of a LCN material with isotropization temperature, T_{iso}, around 123 ^{o}C (the formulation is referred to as Di-C8, being C8 the number of (CH_2) units in the aliphatic chain of sebacic acid[33]). The curing process was carried out as already reported[33]): the mesogenic and the acid were mixed and melted at 180 ^{o}C under magnetic stirring during 10 minutes. Then, the catalyst was added and the whole mixture was rapidly poured in a preheated mold placed inside an oven at 200 ^{o}C. The mold consists of two Teflon-coated metallic plates and a thin Teflon layer placed in between as spacer. A square of 8x8 cm^2 with an exit channel of 2 cm of width to allow gas release was cut in the middle of the Teflon layer. The mixture was left 2 hours and a half to react. After that, films of 250 µm thick were obtained. The reaction scheme and expected network structure of the LCN are shown in Scheme 1.

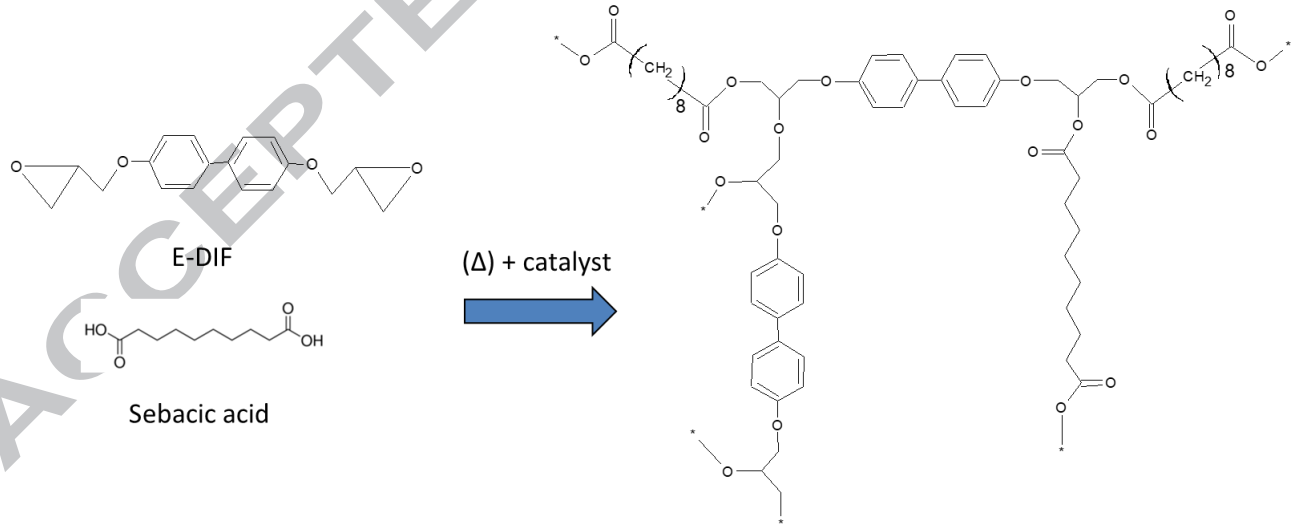

Scheme 1. Reaction scheme and expected network structure of Di-C8 liquid-crystalline network

2.1.2. Actuator stress-applying component: epoxy-based glassy thermoset (GT)

Diglycidyl ether of bisphenol A (DGEBA, GY240, Huntsman, Everberg, Belgium) with an epoxy equivalent weight of 182 g/eq. was used as epoxy resin. Trimethylolpropane tris (3-mercaptopropionate) (S3, Sigma-Aldrich, St. Louis, MO, USA) with a thiol equivalent weight of 132.85 g/eq. was used as curing agent in an under-stoichiometric proportion with respect to the epoxy groups in the system. 1-methylimidazole (1MI, Sigma-Aldrich, St. Louis, MO, USA, 82.1 g/mol) was used as catalyst in a proportion of 1 phr (parts of catalyst per hundred parts of the whole mixture). The DGEBA was dried under vacuum overnight at 80 ºC before use. The other reagents were used as received without further purification.

As it was reported in our previous work, off-stoichiometric "thiol-epoxy" mixtures with epoxy excess catalyzed by tertiary amines can lead to sequential dual-curing systems under the following curing conditions[32,34]. First, the mixture was allowed to react during 1 hour and 45 minutes at 50 ºC for the "thiol-epoxy" polycondensation to take place (1st curing stage). After that, the temperature was increased up to 120 ºC to trigger the homopolymerization of the epoxy excess (2nd curing stage) and was kept at that temperature for 2 hours for the reaction to be completed. In this work, the "intermediate" material (after 1st curing stage) is joined to the shape-shifting component through the 2nd curing stage, thus, the 2nd curing temperature has been lowered to 90 ºC and the time extended to 6 hours to ensure the completion of the epoxy homopolymerization, in order to avoid overpassing T_{iso} (shape-shifting temperature), and therefore making the embedding process under safe conditions. This system is referred to as S3-DGEBA-1MI-r, where "r" is the thiol-epoxy ratio[32,34]. The reaction scheme of both, 1st and 2nd curing stages, and the expected networks of both, intermediate and final materials, are shown in Scheme 2.

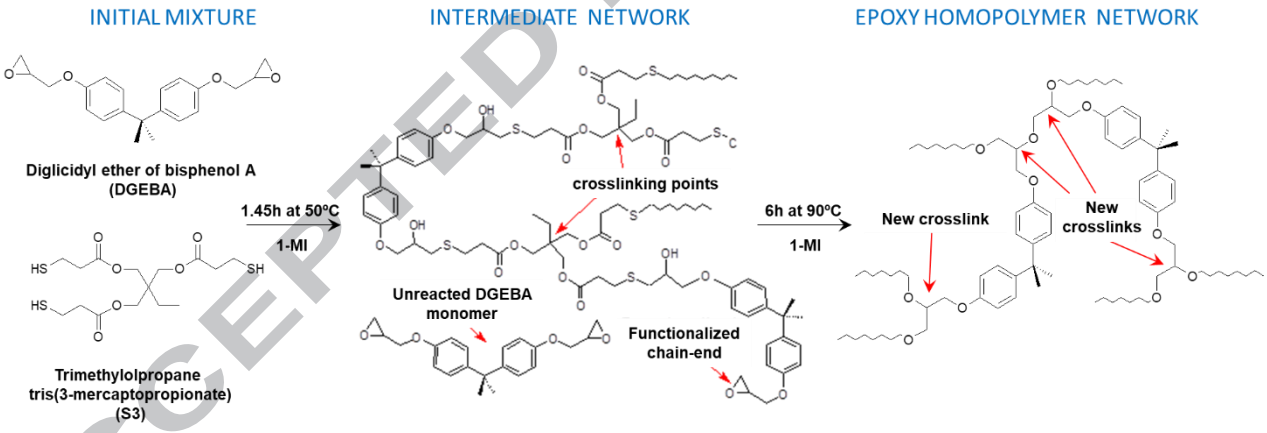

Scheme 2. Reaction scheme and expected network of the intermediate and final materials obtained from the off-stoichiometric "thiol-epoxy" system studied

2.2. Actuator assembling process

In Figure 1 the assembling process of the actuator is schematized. The shape-shifting component is set up by programming the LCN material and fixing the final stretched shape (Figure 1(a)). A Q800 DMA device (TA Instruments, New Castle "DE") equipped with a tension-film clamp in force-controlled mode is used for that purpose, following the same procedure as in our previous work[33]: a temperature of T_{iso}+20 ºC is imposed during 5 minutes for thermal stabilization, followed by a ramp of 10 mN/min up to

a specific % value of the stress at break (programming level, σ_{prog}); afterwards, the temperature is decreased down to 40 °C at 2 °C/min while maintaining the force applied (induced-elongation); finally, the shape is fixed by unloading at 10 mN/min. The programmed LCN is then cut in strips of 20 x (3.5 – 4) mm^2 effective length x width. Films of the GT "intermediate" material of different thickness (120 and 240 µm) are obtained after the 1st curing stage (Figure 1(b)) as explained in the previous section, and are cut in strips longer and wider than the LCN ones (25 x 5 mm^2) to ensure that the whole surface of the LCN is in contact with the GT after joining the two materials (Figure 1(c), top). In Figure1(c), (bottom) an assembly consisting of one layer of GT of 120 µm placed at the bottom (Layer 1), the programmed LCN layer placed in the middle (Layer 2) and a combination of GT layers of 120 and 240 µm up to the desired thickness placed on top (Layer 3) are assembled. The assembly is then confined using Teflon layers and slightly fastened between Teflon-coated glass plates. Finally, the 2nd curing stage of the GT material is carried out and the resulting material is cut and polished Figure 1(d), top, until all layers have equal width x length dimensions leading to the desired actuator configuration Figure1(d), bottom. Note that the combination of GT layers on the top is referred to one thick layer (Layer 3) after the 2nd curing stage.

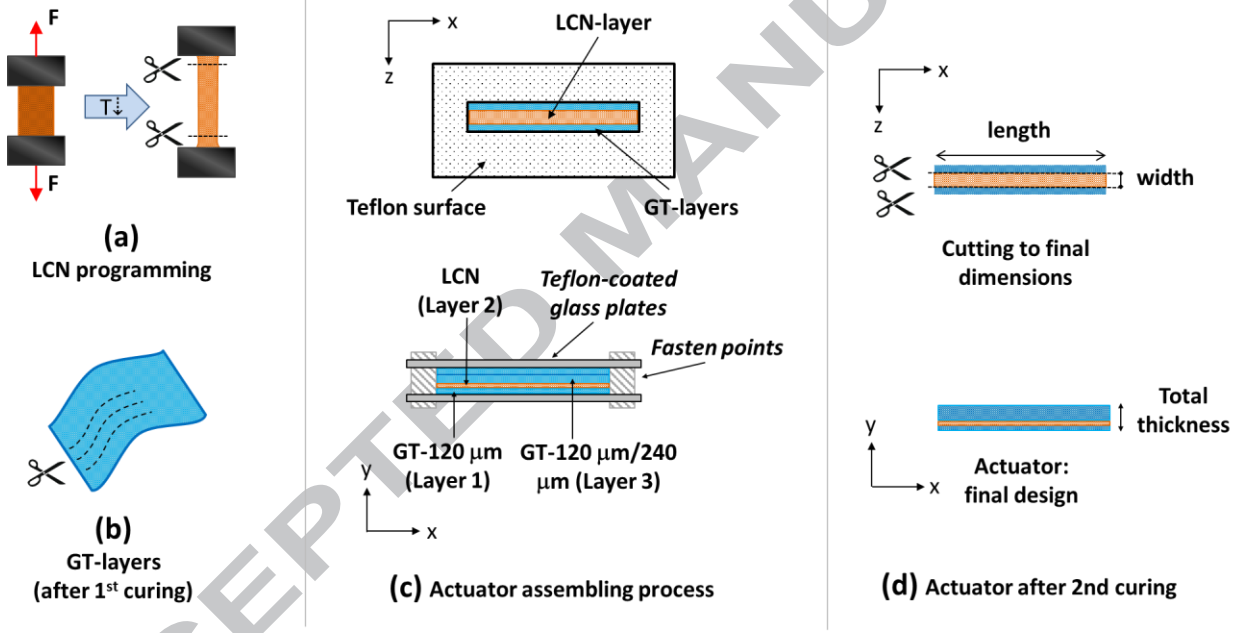

Figure 1. Actuator assembling process: (a) programming and design of the LCN-layer; (b) curing and design of thin GT-layers; (c) configuration; (d) actuator assembly after final curing of the GT

2.3. Characterization of the actuator response

In Figure 2(a), the actuator design is presented in 3D and in the XY plane views. Several actuators, with different configurations and LCN programmed strain levels, were studied. The different configurations were obtained by increasing the thickness of the GT layers on the top (t_{L3}) and the volume fraction, v_F, is calculated as the relation between the GT material ($V_{GT} = V_{L1}+V_{L3}$) and the actuator ($V = V_{L1}+ V_{L2}+V_{L3}$).

$$v_F = \frac{V_{GT}}{V} = \frac{t_{GT}}{t} \quad (1)$$

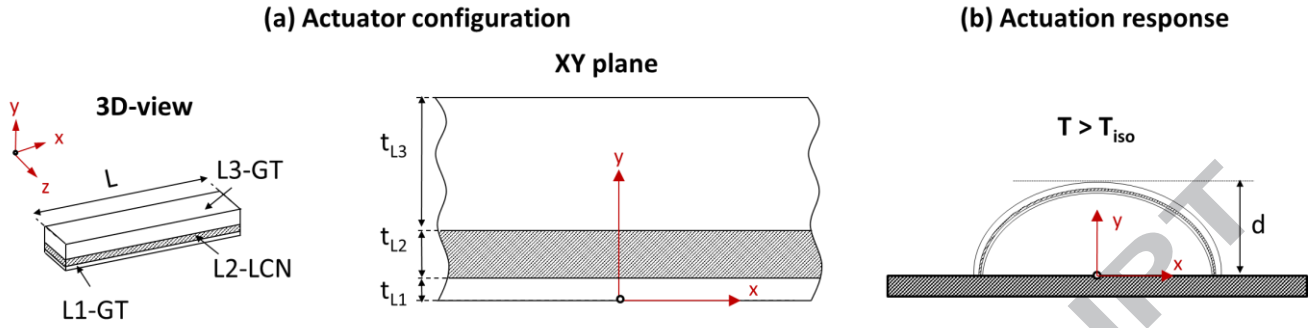

Figure 2. (a) Actuator configuration (3D and XY plane views); (b) Actuation response

Assuming the actuator as a multilayered beam (a detailed explanation is provided in the analytical model section), the actuator will bend upon LCN shrinkage ($T > T_{iso}$) and unbend during the LCN induced-elongation ($T < T_{iso}$), according to Figure 2(b). The *Actuation* can be defined as the quotient between the deflection reached after bending, d, and the theoretical maximum deflection (d_{max}) as follows:

$$Actuation = \frac{d}{d_{max}} \quad (2)$$

$$d_{max} = \frac{L}{\pi} \quad (3)$$

Where L is the length of the actuator and the maximum deflection is that corresponding to an angle of curvature of 180º.

The deflection reached, d, was determined experimentally and under an analytical method. The experimental analyses were carried out using the DMA equipment in the force-controlled mode equipped with a custom-made clamp geometry (see Figure S4 in Supporting Information). A constant force of 0.01 N was imposed in order to follow up the actuator motion. Ten heating-cooling consecutive cycles (1st heating from 30 ºC up to T_{iso}+20 ºC, then heating-cooling from 80 ºC to 140ºC (≈T_{iso}+20 ºC)) were carried out at a constant rate of 2 ºC/min and the displacement of the clamp was recorded as a measure of the instantaneous deflection. In addition, the actuation capability of some of the prepared devices was tested using an oven, by heating up to 150 ºC and naturally cooling down (low cooling rate). The process was visualized by a camera placed in front of the oven door (equipped with a transparent glass window) and the recorded images of the actuator motion are presented in the results section. For actuators with angles of curvature > 180º, the deflection was determined from the visual test, through the angle of curvature (the DMA was unable to follow the actuator motion). Finally, an illustrative video of the response of various actuators upon a heating-cooling cycle is presented in the Supporting Information (Video S1).

For developing the analytical model, the thermo-mechanical properties of both GT and LCN materials have been determined through dynamic-mechanical and thermo-mechanical analyses using the DMA equipment in tension-film clamp geometry. The dynamic-mechanical analyses were performed at a frequency of 1 Hz and 0.1% of strain amplitude. The glass transition temperature, T_g, and isotropization temperature, T_{iso}, were determined as the peaks of the tanδ curve after each relaxation process. The glassy, E_g, liquid-crystalline, E_{lc}, and rubbery, E_r, moduli were determined from the storage modulus

plateau in each thermal region. The coefficients of thermal expansion (CTE) of the materials were also determined by DMA in the force-controlled mode. The samples were heated up to T_g + 30ºC (for the GT material) and T_{iso} + 30ºC (for the LCN material), cooled down rapidly and heated up again at 2 ºC/ min at a constant force of 0.001 N. The CTEs were determined as the slope of the strain-temperature curve (%/ºC) at the different thermal regions (α_g, α_{lc} and α_r) of the second heating curve.

2.4. Morphological analysis

Scanning Electron Microscopy (SEM) analysis have been carried out with a FEI Quanta 200 FEG (Hillsboro "OR" Eindhoven, The Netherlands) in high vacuum mode, using a secondary electron detector and an accelerating voltage ranging between 15 and 20 kV. The cryogenic fractures of different actuators have been analyzed in order to investigate the adhesion between the layers. The most relevant images have been presented and discussed.

3. ANALYTICAL MODEL

Considering the actuator as a multilayered beam with "*n*" layers subjected to a thermal load (ΔT), the mismatch between the layers produced by the generation of different "stress-free" strains is accommodated through a bending deformation according to the multilayered beam theory (see illustration in Figure 3(b))[37,38].

In the present case, "stress-free" strains (ε^0) are given by the combination of the thermal expansion (ε^{th}) and the LCN-shrinkage (ε^{prog}). The "stress-free" strains are additive and define the change in volume of each layer. The thermal expansion is a growing-strain that depends on the material thermal properties. Assuming that the coefficients of thermal expansion "α" are constant in each thermal region "j"[35] (i.e. glassy and rubbery regions), the total ε^{th} suffered by each layer "i" can be expressed as follows (Eq. 4):

$$\varepsilon_i{}^{th} = \sum_{j=1}^{m} \alpha_{j,i} \cdot \Delta T_{j,i} \qquad (4)$$

On the other hand, ε^{prog} is associated to an external strain and therefore is a built-in strain of the layer that must be calibrated externally (in the present case it corresponds to the programmed strain level, thus, the nomenclature refers to "programmed strain"). The total "stress-free" strain suffered by each layer is then expressed as:

$$\varepsilon_i{}^{0} = \varepsilon_i{}^{th} + \varepsilon_i{}^{prog} \qquad (5)$$

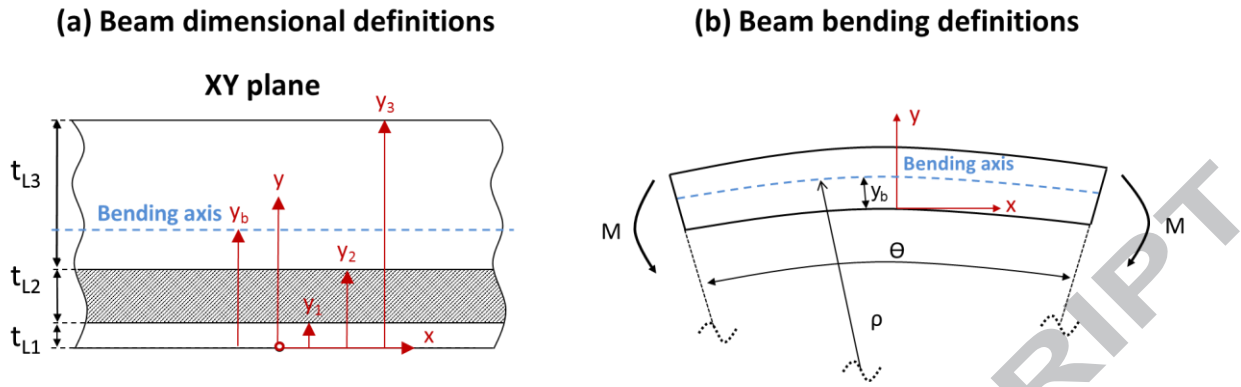

Figure 3. Geometrical definitions of the layered beam: (a) Dimensional definitions; (b) Bending definitions

Assuming that the actuator is a perfect beam (length >> transversal section), that the transversal section remains unchanged after deformation and that the interaction between layers is perfect (the beam behaves as a unity), the study can be reduced to a one-dimensional geometry, in which only variations in the "x" direction (length direction) are considered. In Figure 3(a) the geometrical definitions are presented: the "y-axis" zero position has been placed at the bottom of the beam, thus, the position of each layer, y_i, is defined as the sum of the thickness of all layers below plus its own ($y_i = \sum_i^n t_i$). The position of the bending axis (axis in which the bending strain is null) has been refereed as y_b. After bending, the curvature, κ, the radius of curvature, ρ, and the angle of curvature θ have been defined as indicated in Figure 3(b). For small deformations, κ, ρ and θ are related through the length "L" of the beam as follows:

$$\theta = L\kappa = \frac{L}{\rho} \tag{6}$$

As detailed in the Supporting Information, the normal strain in each layer can be related to the curvature of the beam through the Euler-Bernoulli theory. Adding the contribution of the "stress-free" strains, the total strain in each layer, ε_i, can be expressed relative to the bending axis as follows:

$$\varepsilon_i = {\varepsilon_i}^{elastic} + {\varepsilon_i}^0 = C + (y - y_b)\kappa \tag{7}$$

Where super index *elastic* refers to the total elastic strain and "C" is a constant value related to the uniform strain generated on each layer after geometrical equilibrium (a detailed explanation is provided in the Supporting Information). The stress-strain relation is then approached on applying the Hooke's law to the elastic strain, $\varepsilon_i^{elastic}$:

$$\sigma_i = E_i \cdot \left((y - y_b)\kappa + C - {\varepsilon_i}^0\right) \tag{8}$$

Where E_i is the modulus of each layer (E_i is assumed constant in each thermal region). After applying the equilibrium conditions (force and moment balances) in each layer, κ and y_b are related as follows:

$$\sum_{i=1}^{n}\int_{y_{i-1}}^{y_i}\sigma_i dy = \sum_{i=1}^{n}\left(\int_{y_{i-1}}^{y_i}E_i y dy - \int_{y_{i-1}}^{y_i}E_i y_b dy\right)\cdot\kappa + \int_{y_{i-1}}^{y_i}E_i C dy - \int_{y_{i-1}}^{y_i}E_i {\varepsilon_i}^0 dy = 0 \quad (9)$$

$$\sum_{i=1}^{n}\int_{y_{i-1}}^{y_i}\sigma_i y dy = \sum_{i=1}^{n}\left(\int_{y_{i-1}}^{y_i}E_i y^2 dy - \int_{y_{i-1}}^{y_i}E_i y_b y dy\right)\cdot\kappa + \int_{y_{i-1}}^{y_i}E_i C y dy - \int_{y_{i-1}}^{y_i}E_i {\varepsilon_i}^0 y dy = 0 \quad (10)$$

Solving Eqs.9 and 10, the curvature, κ, can be expressed as a function of different constants as follows:

$$\kappa = \frac{A(M_{SR}+M_{th}) - B(F_{SR}+F_{th})}{AB - D^2} \quad (11)$$

where A, B and D refers to the extensional, bending and coupling constants respectively in terms of laminated composite materials. F_{th} and M_{th} denote respectively the force and moment generated by the thermal expansion "stress-free" strain and F_{SR} and M_{SR} to the LCN shrinkage "stress-free" strain (all the constants are developed in the Supporting Information).

Using the κ, ρ and θ relations (see Eq.6), the deflection, d, can be approached by trigonometry as follows:

$$d\ (\theta < 180^o) = \rho\cdot(1-\cos\frac{\theta}{2}) \qquad d\ (360^o > \theta > 180^o) = \rho \quad (12)$$

Note that for an angle of curvature higher than 180º, the deflection is defined as the radius of curvature, meaning that it decreases as the circle (360º) is being formed. It must be acknowledged that such bending level is out of the elastic theory limits (small deflections); however, it is considered for further discussion with the experimental results. Finally, the *Actuation* is determined using Eq. 2:

$$Actuation = \frac{d}{d_{max}} = \frac{\rho\cdot\left(1-\cos\frac{\theta}{2}\right)}{L/\pi} \quad (13)$$

From the equation above it is deduced that the maximum deflection is reached for an angle of 180º by definition, whereas, higher angles of curvature lead to lower *Actuation*.

4. RESULTS AND DICUSSION

As stated in the introduction, free-standing, reversible actuation is attained by the incorporation of a compatible stress-applying component into the shape-shifting component[25]. In this work, an epoxy-based glassy thermoset, GT, is used as external stress-applying component and an epoxy-carboxylic LCN stretched up to a certain strain level (programmed strain, ε_{prog}) is used as the shape-shifting component.

The thermo-mechanical compatibility between components is achieved by adjusting the T_g of GT below the T_{iso} of the LCN, to ensure that GT is in the rubbery state ($T > T_g$) during the LCN shrinkage, thus allowing further LCN elongation thanks to the GT elastic response[27].

Taking into account the above, the T_g of the GT material must be lower than 121 ^oC (T_{iso} of the LCN material). Another important consideration is that the GT intermediate material (after the 1st curing stage) must be solid-like and deformable to allow the processing of strips before the assembling process. As it was reported in our previous work[34], the physical and structural properties of the GT material are controlled with the thiol-epoxy ratio. For this particular system, a ratio > 0.65 (minimum ratio to form a gelled structure after the 1st curing stage) leads to solid-like and deformable intermediate materials that after the 2nd curing stage reach T_g values ranging from 70 ^oC to 34 ^oC. In addition, it was demonstrated that using ratios slightly below this critical ratio also leads to solid-like materials, enhancing the deformability and stickiness. These materials are interesting due to their liquid-like behavior, which is expected to enhance the adhesion between the LCN and GT layers[39].

Therefore, a S3-DGEBA-1MI system with a "thiol-epoxy" ratio of 0.6 has been chosen as the GT material of study. This system leads to a final material with a T_g lower than T_{iso}, as will be later shown.

4.1. Determination of the model parameters

Once the stress-applying GT and the LCN have been selected, their structural and thermal properties were determined as detailed in the experimental section. The results are summarized in Table 1.

Table 1. Formulation, dynamic-mechanical and thermal properties of the GT and LCN materials

Material	Nomenclature	E_g (MPa)	E_{lc} (MPa)	E_r (MPa)	α_g ($^oC^{-1}$)	α_{lc} ($^oC^{-1}$)	α_r ($^oC^{-1}$)	T_g (^oC)	T_{iso} (^oC)
GT	S3-DGEBA-1MI-0.6	2150 ± 50	---	16.8 ± 0.3	$3.4 \cdot E^{-5}$	---	$2.0 \cdot E^{-4}$	71 ± 2	---
LCN	Di-C8	1340 ± 50	10 ± 1	2.9 ± 0.2	$1.0 \cdot E^{-4}$	$3.0 \cdot E^{-4}$	$7.6 \cdot E^{-5}$	54 ± 2	121 ± 3

As stated in the experimental section, the LCN films were stretched up to a certain % of the stress at break, σ_b, in order to program the shape-shifting component. Here, five levels of programming have been chosen for a preliminary analysis of the actuator response with the model (σ_{prog} = 1%, 2%, 5%, 10% and 25% of σ_b). The results are presented in Figure 4.

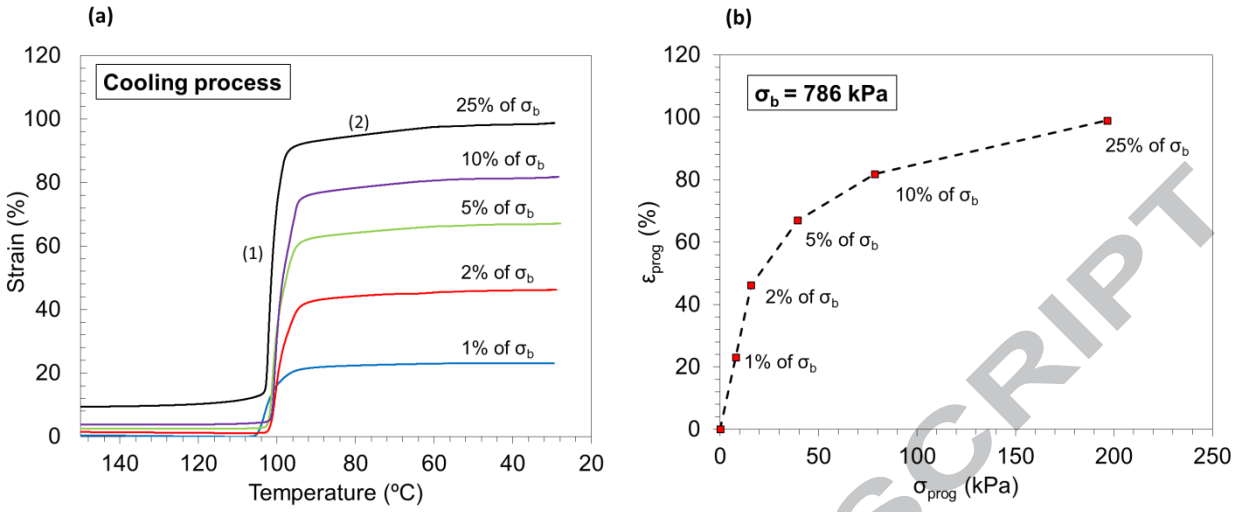

Figure 4. LCN programming at different stress levels (from 1% to 25% of stress at break); (a) Strain as a function of the temperature; (b) Programmed strain as a function of the programming stress

In Figure 4(a), the strain evolution is plotted as a function of the temperature during the cooling step, whereas in Figure 4(b), the relation between the programming stress, σ_{prog}, and programmed strain, ε_{prog}, is shown (σ_b has been highlighted in the graphic). As can be observed, the programmed strain (determined as the maximum strain reached after cooling down) increases with the increase of the programming stress level with no linear trend: at low programming level, from 1% to 5% of σ_b, the increase in programmed strain is much higher than from 5% to 25% of σ_b as deduced in Figure 4(b). This can be explained as follows: the induced-elongation (step (1) in Figure 4(a) is related to the soft elasticity, where the configurational change of the network (formation of the LC domains) on cooling below T_{iso}, allows stretching with minimal force (formation of a monodomain aligned in the load direction)[40]. Of course, this process is time-temperature dependent. In our case, the cooling rate is fixed, however the force applied depends on the programming level and therefore the stretching rate increases with the programming level (these experiments were carried out in force-controlled mode). High stretching rates may lead to network relaxation phenomena taking place during the stretching process, thus, slowing down the process[33]. If one analyzes the strain evolution after the induced-elongation (step (2) in Figure 4(a), it is clear that higher programming levels result in a constant increase of the strain associated to some residual relaxation of the network taking place at $T < T_{iso}$. This would explain the incomplete network relaxation during the induced-elongation, step (1), and therefore, the nonlinear trend observed. However, in our previous work[33] we demonstrated that high shape-memory cycling stability is attained when programming at 25% of σ_b, therefore we do not expect a great influence of the programmed stress on the actuator stability.

4.2. Model Output: Preliminary analysis

The model parameters for the case of study are summarized in Table 2. As stated in the analytical section, the actuator is subjected to a thermal load, ΔT, which is responsible for two different phenomena: the thermal expansion of the different layers and the shrinkage of the LCN layer. While the strain related to the LCN shrinkage is a constant parameter in the model, the strain associated to the

thermal expansion depends on the thermal load. In the present case, the thermal expansion generated from room temperature up to 90 ºC is neglected since the assembling process was carried out at 90 ºC, thus, the corresponding thermal history is already included in the actuator at room temperature and eventually erased after reaching 90 ºC (the zero point is placed at 90 ºC). Therefore, the temperature gradient is defined from 90 ºC up to 140 ºC (in Table 2, the thermal load is divided in the different thermal regions according to the transition temperatures of each material).

Table 2. Model parameters for the case of study: actuator geometry (thickness and length), thermal load and programmed strain

Layer	Material	t (mm)	L (mm)	ΔT_g [b] (ºC)	ΔT_{lc} [b] (ºC)	ΔT_r [b] (ºC)	ε_{prog}
L1	GT	0.12	20	0	0	50	0
L2	LCN	[0.19 - 0.23][a]	20	0	31	29	[-0.23 - -0.81]
L3	GT	[0.12 - 5]	20	0	0	50	0

a) The thickness of the LCN layer depends on the programmed strain level

b) "g", "lc" and "r" sub-indexes refer to the glassy, liquid-crystalline and rubbery regions respectively

Four different programmed strain levels (ε_{prog} = 23%, 43%, 71% and 81%) corresponding to a programming stress level of 1%, 2%, 5% and 10% of σ_b (see Figure 4) have been used in the model. Each programmed strain level has been applied for different configurations through the variation of t_{L3} (from t_{L3} = 0.12 corresponding to $v_F \approx 0.5$ to t_{L3} = 5 mm, $v_F \approx 1$), in accordance with the proposed actuator design (see Figure 2(a)) and Eq. 1. The length of the actuator has been defined as 20 mm and the width neglected since it is eventually simplified in the model.

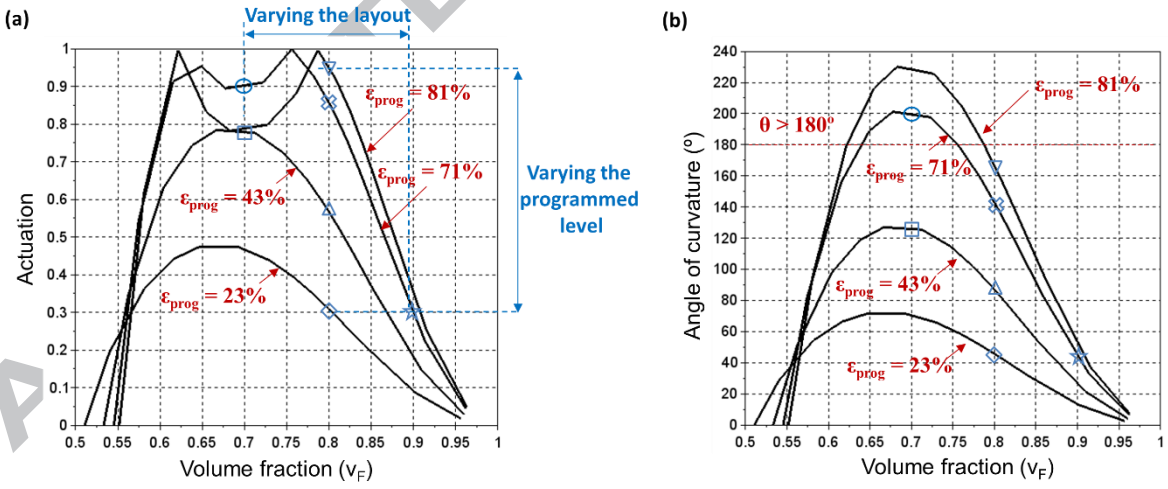

Figure 5. Model output: (a) *Actuation* and (b) angle of curvature as a function of the volume fraction at different programmed strain levels. The blue markers indicate the experimental assemblies to be tested (they are not experimental results)

The results of the model are shown in Figure 5: the *Actuation* (Figure 5(a)) and the angle of curvature (Figure 5(b)) are presented as a function of the volume fraction (different actuator configurations) for the different programmed strain levels (different curves). As it can be observed, the *Actuation* strongly depends on both the programmed strain level and the volume fraction. Starting from a theoretical $v_F = 1$ ($t_{L3} \approx$ infinite), point at which the *Actuation* would be null, on decreasing v_F, that is, decreasing t_{L3}, the *Actuation* increases up to a maximum value (see Figure 5(a)). If the sum of the "stress-free" strains is low enough to avoid angles of curvature > 180º (see in Figure 5(b)), this maximum is placed at $t_{L3} = t_{L2} + t_{L1}$ (geometrical equilibrium); from this point to lower volume fractions there is a progressive decrease of the *Actuation* as t_{L3} approaches t_{L1} (i.e. at ε_{prog} = 23% and 43%) point at which there is no "bending" *Actuation* (theoretically, the beam would suffer a planar shrinkage). From this v_F (i.e. $v_F \approx 0.55$ for the ε_{prog} = 81% curve) to lower volume fractions the *Actuation* curve would be the same but in the opposite direction (an inversion of the *Actuation* because the curvature of the beam, κ, becomes negative). When the "stress-free" strains produce angles of curvature > 180º (i.e. at ε_{prog} = 71% or higher), the deflection is equal to the radius of curvature (see Eq. 3), therefore, the *Actuation* is maximum at θ = 180º and decreases at higher angles of curvature. Because of the geometrical equilibrium is found at θ > 180º, there is a minimum instead, and two maximum values appear at θ = 180º.

Overall, the model predicts that it is possible to control the *Actuation* by modifying the actuator configuration and the LCN programmed strain level. This is of utmost importance when designing the actuator. The thickness of the GT layers defines the stiffness of the actuator, thus, the potential capabilities as a mechanical actuator, as well as the actuation design. Therefore, for a given configuration, the *Actuation* can be optimized by modifying the programmed strain level in an easy and efficient manner. Moreover, this can be extended to the variation of the thermo-mechanical properties of both materials. The model is able to predict the response depending on the materials properties, thus, it is possible to modulate both the stiffness and *Actuation* thanks to the versatility of the proposed materials: in the GT material, the network structure can be controlled through the "thiol-epoxy" ratio as well as the "thiol-epoxy" system[11,34], whereas, in the LCN material, the rubbery modulus and isotropization temperature can be easily tailored by varying the aliphatic chain length of the acid curing agent as proposed in a previous work[33].

In order to verify the model predictions, an experimental investigation of the actuators varying the configuration and LCN programmed strain level has been carried out. In Figure 5, the blue markers indicate the experimental actuators assembled and analyzed (they are not experimental results). As it can be seen, a wide range of possible responses is covered: from low level of *Actuation* (corresponding to a $v_F = 0.9$) to high level of *Actuation* (for $v_F = 0.7$). As stated earlier, angles of curvature > 180º (i.e. the point $v_F = 0.7$ with ε_{prog} = 71%) are probably out of the model limits of applicability, however, it is worth analyzing the real behavior and compare it with the model predictions.

4.3. Actuator response: experimental analysis

The proposed actuator configurations have been assembled as explained in the experimental section. The dimensional parameters and LCN programmed strain levels are summarized in Table 3. Note that the nomenclature of the actuators refers to the volume fraction (i.e. "07" means $v_F = 0.7$) and the programming stress (i.e. "1%" is σ_{prog} = 1% of σ_b). In Table 3, it is worth noting the variation of some

parameters, such as the total thickness (t) and the LCN programmed strain level (ε_{prog}). As the purpose of this study is to analyze different geometrical configurations and different LCN programmed strain levels, we had defined the parameter v_F as a non-dimensional factor eliminating the geometrical variation in thickness and making possible to vary the configuration in a controlled way. On the other hand, the variation in programmed strain (ε_{prog}) is similar to the error found in typical stress-strain experiments. The variation of the width is not relevant if the actuator accomplishes the geometrical relation for a beam-like design, and the variation of ± 1 mm in length is taken into account in the model and will be discussed later.

Table 3. Dimensions and programmed strain for the actuators of study

Actuator	v_F	t_{L1} (mm)	t_{L2} (mm)	t_{L3} (mm)	t (mm)	w (mm)	L (mm)	ε_{prog} (%)
A_08_1%	0.808 ≈ 0.8	0.12	0.23	0.85	1.20 ± 0.01	3.0 ± 0.1	20.0 ± 0.1	23.0
A_08_2%	0.809 ≈ 0.8	0.12	0.21	0.77	1.10 ± 0.01	3.5 ± 0.1	20.8 ± 0.1	49.3
A_08_5%	0.820 ≈ 0.8	0.12	0.20	0.79	1.11 ± 0.01	3.9 ± 0.1	19.2 ± 0.1	70.0
A_08_10%	0.805 ≈ 0.8	0.12	0.20	0.69	1.00 ± 0.01	4.2 ± 0.1	20.5 ± 0.1	81.0
A_07_2%	0.697 ≈ 0.7	0.12	0.22	0.37	0.71 ± 0.01	3.9 ± 0.1	19.0 ± 0.1	43.0
A_07_5%	0.717 ≈ 0.7	0.12	0.21	0.40	0.72 ± 0.01	3.4± 0.1	20.1± 0.1	71.0
A_09_5%	0.903 ≈ 0.9	0.12	0.20	1.72	2.03 ± 0.01	4.1 ± 0.1	20.6 ± 0.1	70.1

In Figure 6, photographs of the assembling process of A_08_5% are shown. As can be observed, after the 2nd curing stage (Figure 6(c)), the length of the LCN-layer remains unchanged; pointing out that no recovery took place during the 6 hours at 90 °C. After polishing, the position of the LCN layer (indicated in Figure 6(d)) can be clearly distinguished. If one analyses the frontal view, it can be reasonably said that the desired configuration has been successfully achieved. It is worth noting that the actuator is slightly bent upwards (see Side view in Figure 6(d)). This can be rationalized as follows: during the 2nd curing stage of the GT layers (assembling process), the epoxy homopolymerization takes place. As described in[41], this reaction generates internal stresses caused by shrinkage that, under constrained conditions and after cooling down to room temperature, lead to a final bending of the material (Note that $t_{L3} > t_{L1}$, thus the beam contracts on the top).

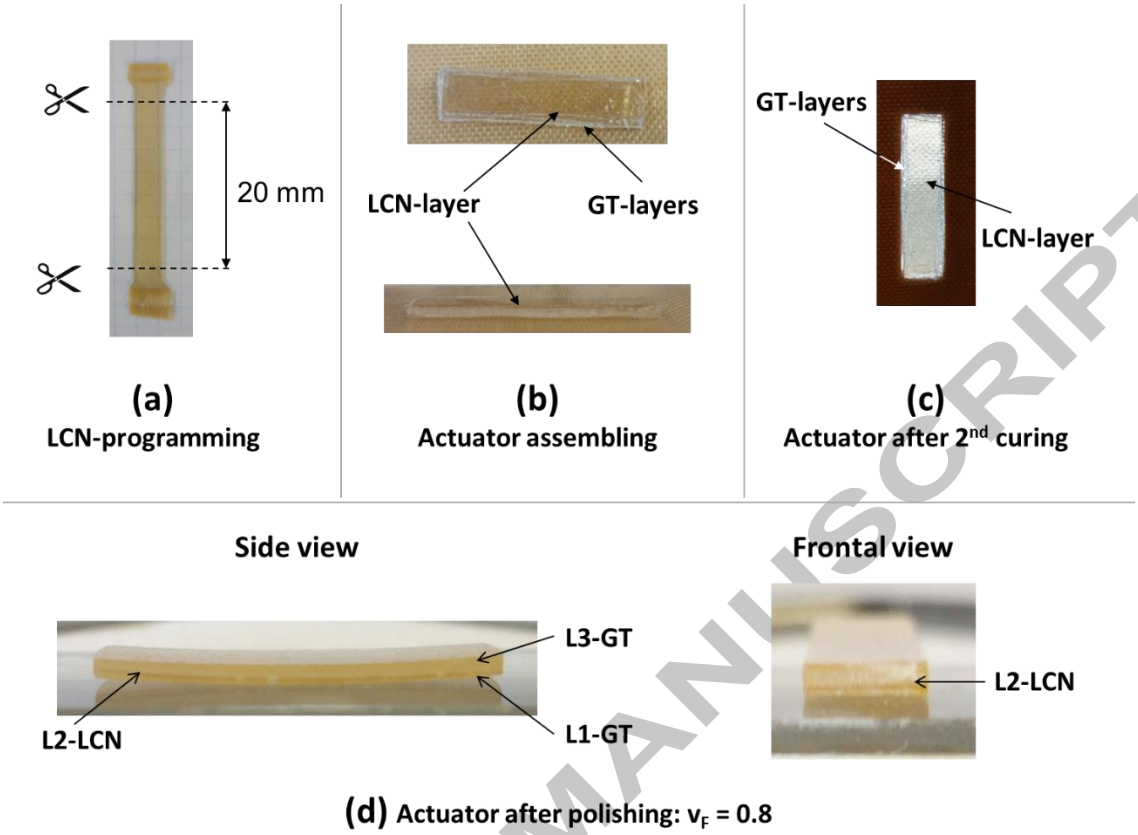

Figure 6. Photographs of the actuators assembling process

In order to analyze the adhesion efficiency of the layers, In Figure 7, SEM images of the cryogenic fracture of A_08_2% are shown. From Figure 7(a) to Figure 7(c), the whole thickness (Figure 7(a)), magnifications of the LCN layer (Figure 7(b)) and the interface between the LCN and GT layers (Figure 7(c)) are presented. In Figure 7(a), it can be confirmed that, after the assembling process the GT layers were completely mixed in one thicker and homogeneous block as deduced from the absence of interface lines between them. The use of "thiol-epoxy" ratios close but slightly below the critical ratio (r ≤ 0.65) produces an initial and slight softening of the material that, thanks to the slight pressure applied by the glass plates during the assembling process, promotes an efficient wetting of the LCN layer and effective inter-layer adhesion before the reaction takes place, therefore allowing the formation of a unique block[34]. Figure 7(b) points out the differences between an amorphous network, the GT, where the fracture is homogeneous and smooth, and a liquid-crystalline network, the LCN layer, where several cracks are formed and deviated due to the presence of LC domains[42]. Finally, in Figure 7(c) evidences of crack propagation are clearly appreciated: the cracks propagate from the LCN to the GT layers pointing out the strong adhesion between them. Probably, not only physical bonds are formed during the assembling process, but also chemical bonds between the epoxy monomers of both materials are created.

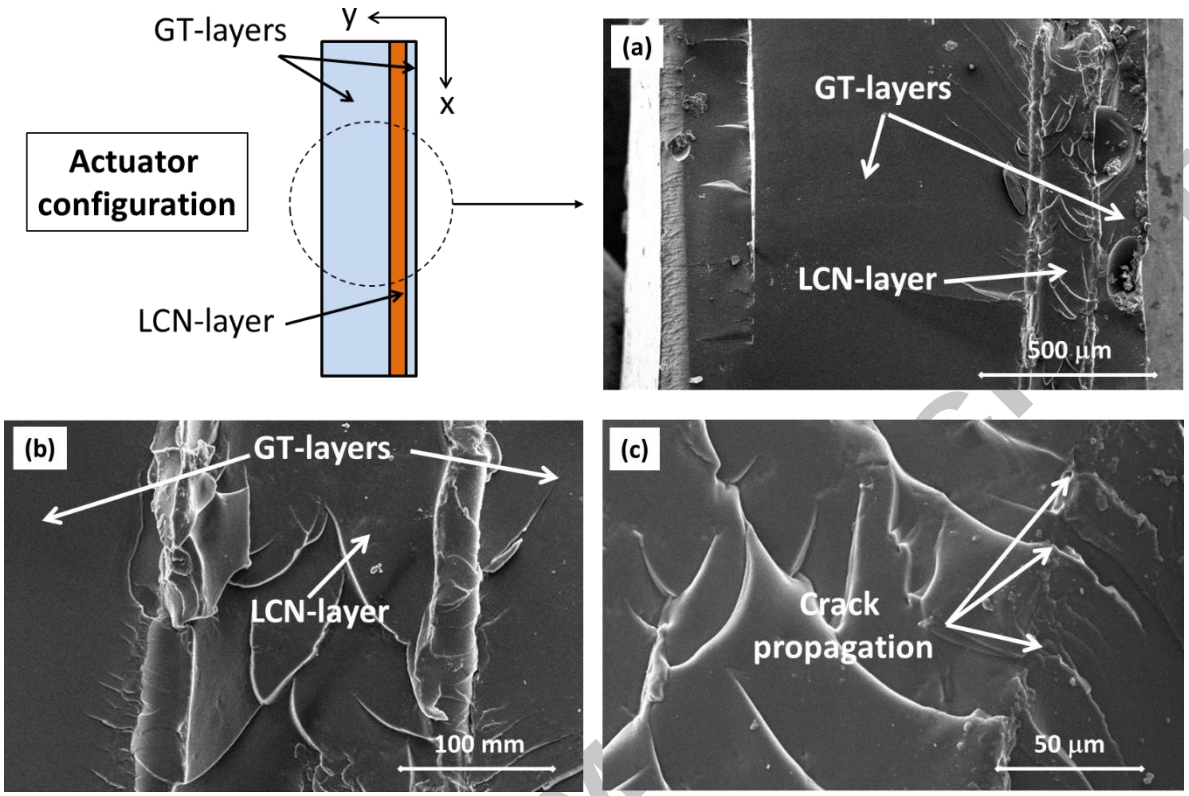

Figure 7. SEM images of the cryogenic fracture of the actuators

The results of the actuators response measured by DMA are summarized in Table 4 and the actuation cycles of A_08_1% are presented in Figure S4 in Supporting Information. In addition, images of the actuation process are shown in Figure 8 and an illustrative video is provided in the Supporting Information (Video S1). As it can be observed, in all cases, on heating above T_{iso} (Figure 8(e)), the actuator is able to bend up to a certain deflection level (metastable "state-of-ease" shape), while it goes back to the initial shape on naturally cooling down to T_{room} (Figure 8(a)). This process is repeated several times until a stable cycling is reached and therefore, the operational design of the actuator is defined (see the actuation stability attained after 8-10 cycles in Figure S4).

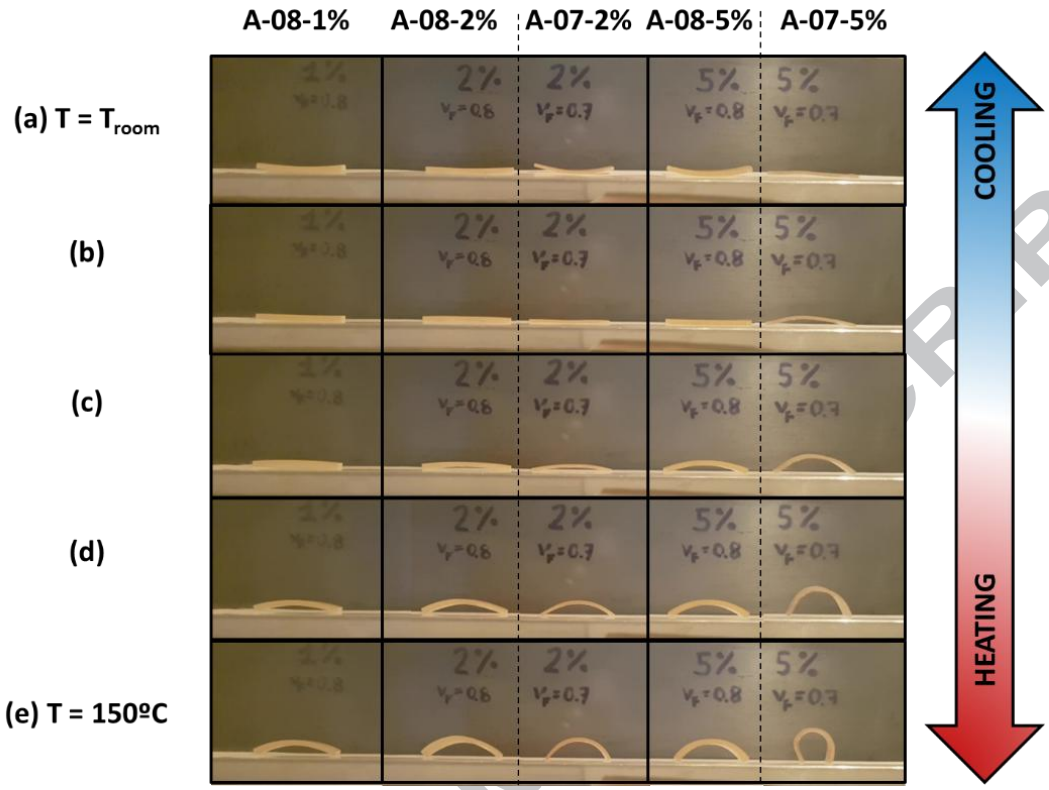

Figure 8. Actuation response: visual demonstration of the different configurations studied

Table 4. Parameters of the actuator response characterization

Actuator	v_F	L (mm)	d (mm)	d_{max} (mm)	$Actuation_{exp}$ (%)	$Actuation_{model}$ (%)
A_08_1%	0.808	20.0 ± 0.1	1.77	6.37	27.8	28
A_08_2%	0.809	20.8 ± 0.1	3.77	6.62	56.9	56.0
A_08_5%	0.820	19.2 ± 0.1	4.28	6.09	70.2	71
A_08_10%	0.805	20.5 ± 0.1	6.40	6.51	98.3[b]	96.1
A_07_2%	0.697	19.0 ± 0.1	1.77	6.55	71.9	73.0
A_07_5%	0.717	20.1± 0.1	4.79[a]	6.39	74.9	91.2
A_09_5%	0.903	20.6 ± 0.1	4.35	6.04	27.0	27.5

a) Visual determination through the angle of curvature
b) The LCN split from the GT layer after the first cycle

As can be observed, from room temperature (Figure 8(a)) up to a certain temperature below T_{iso} (Figure 8(b)), the actuators pass from the initial bent shape to a flat shape. This is related to the explanation given above: the curing process and further cooling down to room temperature generates an initial bending that after heating up again is recovered. In order to thoroughly analyze the exact

temperature at which the actuator shape becomes flat, the A_07_2% was tested in the DMA placing it in opposite direction to the actuation, thus, to record the initial unbending until the actuator becomes flat. It was observed that the unbending starts at T ≈ 60 ^{o}C and ends at T ≈ 90 ^{o}C (the 2nd stage curing temperature), thus the assumption in the model of ΔT starting from 90 ^{o}C is in agreement with the experimental observations. After that, on approaching T_{iso}, the actuators bend up to certain deflection (Figure 8 (c)-8(d)-8(e)) that depends on the configuration and LCN programmed strain accordingly to the predictions of the model. It is worth noting that the actuators remain stable until the temperature is lowered below T_{iso} and the flat shape (Figure 8(b)) is recovered due to the induced-elongation of LCN coupled to the elastic response of the GT material. Further cooling down to room temperature allows the actuator to recover its initial shape (Figure 8(a)).

If one analyses the deflection reached, d, in Table 4 and the corresponding *Actuation*, it is clear that the length has a crucial role. As can be seen, due to experimental limitations, the length of the actuators has an error of ± 1 mm (see Table 4) and the *Actuation* is very sensitive to slight changes in length, as deduced from its definition in Eq. 2. For example, from A_08_2% to A_08_5%, the difference in "d" is about 0.5 mm, whereas the *Actuation* increases up to 25%. However, if one compares from A_08_1% to A_08_2%, the difference in deflection is much greater (about 2 mm), but the *Actuation* increases the same level. This is caused by the difference in length (from 20.8 mm to 19.2 mm) between A_08_1% and A_08_5%.

In Figure 9, the experimental data (lighter points) are compared with the results of the model (darker points). As can be observed, the experimental data fit very well with the model predictions (see also Table 4): not only is the tendency similar (the *Actuation* increases with the level of programmed strain and with the decrease of v_F), but also the *Actuation* values are closely related to the theoretical ones. In general, the best data fitting is found at low programmed strain levels (i.e. ε_{prog} = 23% and 43%) and high v_F (i.e. v_F = 0.8 and 0.9). This can be explained as follows: on the one side, the reduction of the programmed strain level leads to lower angles of curvature, thus, obeying the model assumptions related to the linear elasticity. On the other side, the increase of v_F reduces the experimental error when assembling the actuator (increasing the thickness of the actuator makes easier the proper positioning of the LCN layer). On analyzing the actuator A_07_5%, the experimental *Actuation* clearly differs from the model prediction (0.72 against 0.91). Here, the model predicted an angle of curvature of 200^{o} (see Figure 5(b)) which considerably overpasses the model limitations (the model is developed under the basis of small deformations), whereas the visual test showed an angle of 240^{o}. High deformation levels lead to the planar deformation of the transversal section along the length, thus, the model simplifications are not valid anymore. This means that, from a quantitative point of view, the model has no application at such deformation levels; instead, it can be useful to analyze the tendency and avoid such undesired deformation levels.

Although the effect of the structural parameters of the GT and LCN materials with the actuation response is out of the scope of the present paper, it is worth to analyze them from a qualitative point of view. Considering the model predictions, it can be anticipated that increasing the rubbery modulus would lead to lower actuation levels, but increased stiffness of the device during actuation, that means, higher performance as mechanical actuators. However, the variation of the rubbery modulus is related to other parameters such as crosslinking density, network hindrance and T_g. We speculate the possibility to modulate the actuation in terms of rate and stability through the variation of these parameters:

whereas the model is able to predict the actuation level, the relaxation dynamics of the GT material, as well as the dynamics of the LC transition in the LCN, could serve to modulate the actuation path (velocity and shape). For example, approaching the T_g of the GT to T_{iso} of the LCN would cause an overlap of network relaxation with the LCN shrinkage that may slow down the actuation. Further studies on this matter will be done and the possibility to incorporate the effect in the model will be considered.

Finally, it must be acknowledged that all the actuators were able to bear the level of deformation in terms of resistance at break. Nevertheless, in terms of layers adhesion, A_08_10% failed, as the LCN layer separated from the GT layers after the 1st cycle (an image of the actuator disassemble is shown in Figure 9). In contrast, the actuator A_07_5%, with $\theta \approx 240^o$, was able to retain the LCN layer. This suggests that the programmed strain level in the LCN layer is the responsible of the actuator disassemble instead of the *Actuation* or angle of curvature achieved. An approach to enhance the layers adhesion, thus, the performance of the LCN in the assembled device, would be the use of "thiol-epoxy" systems with higher content of epoxy excess during the assembling process, that is, stronger interactions between the GT and LCN surfaces. This would effectively increase the adhesion between layers, making possible to use LCN's with a programmed strain higher than 5% with good performance in the assembled device. However, it must be acknowledged that increasing too much the epoxy content may lead to brittle GT materials, decreasing the maximum actuation of the assembled device. In this study, a GT material with 40% of epoxy excess is used and a bending angle of 240º has been achieved as observed in A_07_5%, therefore, an increase of 10% or 20% of epoxy excess would considerably enhance the layers adhesion, while maintaining sufficient deformability, making possible to attain bending angles of 180º (defined as the maximum operationally effective angle). By increasing the percentage of LCN programmed strain it is expected to modify the actuation response in terms of rate and stability.

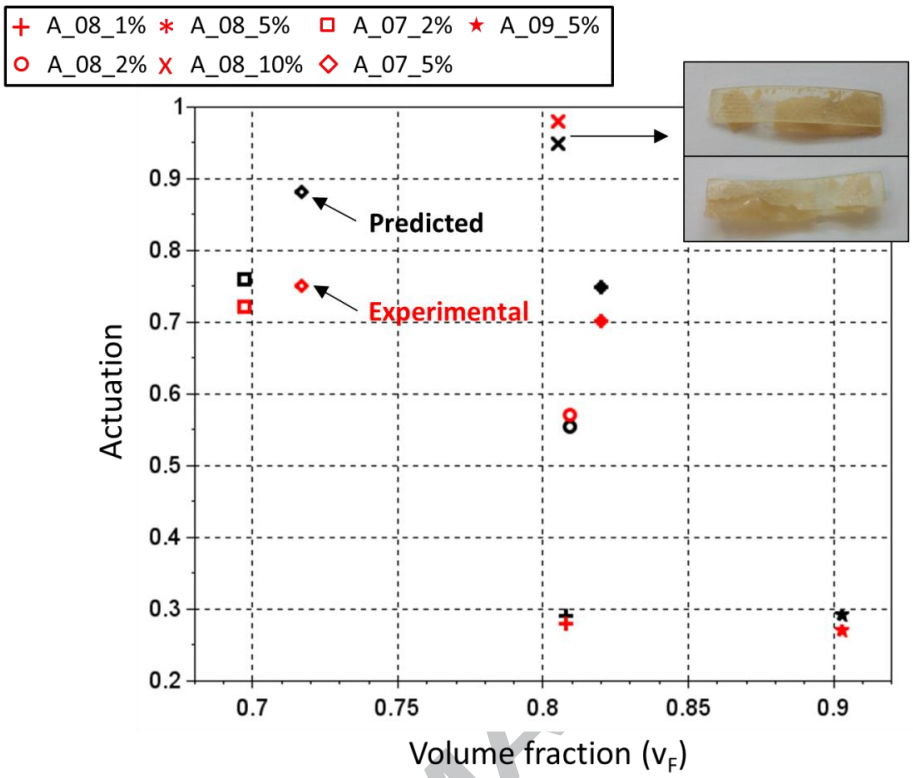

Figure 9. Predicted deflection as a function of the volume fraction at different internal stresses in front of the experimental data.

5. CONCLUSIONS

Actuators with different configurations (GT-LCN-GT) have been successfully assembled through a multilayer methodology. SEM analyses have evidenced strong adhesion between the GT and LCN layers with the presence of crack propagation among them. In addition, from the smooth surface and the absence of layer separation it has been deduced that multiple GT layers forms a single block of GT material after the assembling process, thus, enhancing the actuator mechanical performance.

In all cases, an actuation response has been achieved: the actuator has been able to bend up to a temporary shape on heating above T_{iso} and unbend down to the original shape on cooling down T_{iso}. A model based on the multilayered beam theory to predict the extent of deflection has been proposed and experimentally verified. All the parameters of the model have been determined through dynamic-mechanical and thermo-mechanical analyses and the LCN programmed strain level has been analyzed at different programming stress levels. The results have shown that the increase of the programmed strain with the programming level does not follow a linear trend due to the presence of network relaxation when the induced-elongation is driven too fast. The model has been applied to some of the analyzed LCN programmed strain levels for all possible configurations. Results have shown that the *Actuation* increases with increasing of the programmed strain level, exhibiting a maximum at the geometrical equilibrium between the layers. Nevertheless, angles of curvature higher than 180^o lead to a decrease of the *Actuation*, as the device tended to assume a rounded shape on approaching 360^o. The experimental

results are in good agreement with the model predictions. As a matter of fact, only actuators with angles of curvature higher than 180º deviate from the model output due to the high deformation level, overpassing the model limits of applicability.

ASSOCIATED CONTENT

Supporting Information. A detailed development of the Analytical Model is available in supporting information. In addition, an illustrative video of the actuation response for different actuators is also available.

ACKNOWLEDGMENT

The authors would like to thank MICINN (MAT2014-53706-C03-01 and MAT2014-53706-C03-02) and Generalitat de Catalunya (2014-SGR-67) for financial support. Xavier F.-F. also acknowledges the Serra Húnter programme from the Generalitat de Catalunya..

REFERENCES

[1] A. Lendlein, C. Wischke, K. Kratz, M. Heuchel, J. Zotzmann, B. Hiebl, A.T. Neffe, M. Behl, B. Development, Shape-Memory Polymers, Elsevier Ltd., 2011. doi:10.1016/B978-0-08-055294-1.00271-3.

[2] Q. Zhao, H.J. Qi, T. Xie, Recent progress in shape memory polymer: New behavior, enabling materials, and mechanistic understanding, Prog. Polym. Sci. 49–50 (2015) 1–42. doi:10.1016/j.progpolymsci.2015.04.001.

[3] F. Xie, L. Huang, J. Leng, Y. Liu, Thermoset shape memory polymers and their composites, J. Intell. Mater. Syst. Struct. 27 (2016) 2433–2455. doi:10.1177/1045389X16634211.

[4] J. Leng, X. Lan, Y. Liu, S. Du, Shape-memory polymers and their composites: Stimulus methods and applications, Prog. Mater. Sci. 56 (2011) 1077–1135. doi:10.1016/j.pmatsci.2011.03.001.

[5] A. Lendlein, T. Sauter, Shape-memory effect in polymers, Macromol. Chem. Phys. 214 (2013) 1175–1177. doi:10.1002/macp.201300098.

[6] M. Anthamatten, S. Roddecha, J. Li, Energy storage capacity of shape-memory polymers, Macromolecules. 46 (2013) 4230–4234. doi:10.1021/ma400742g.

[7] C.L. Lewis, Y. Meng, M. Anthamatten, Well-Defined Shape-Memory Networks with High Elastic Energy Capacity, Macromolecules. 48 (2015) 4918-4926. doi:10.1021/acs.macromol.5b00763.

[8] D. Santiago, A. Fabregat-Sanjuan, F. Ferrando, S. De la Flor, Recovery stress and work output in hyperbranched poly(ethyleneimine)-modified shape-memory epoxy polymers, J. Polym. Sci. Part B Polym. Phys. 54 (2016) 1002–1013. doi:10.1002/polb.24004.

[9] A. Belmonte, X. Fernández-Francos, S. De la Flor, À. Serra, Network structure dependence on unconstrained isothermal-recovery processes for shape-memory thiol-epoxy “click” systems,

Mech. Time-Dependent Mater. (2017) 1–17. doi:10.1007/s11043-016-9322-z.

[10] W. Wang, Y. Liu, J. Leng, Recent developments in shape memory polymer nanocomposites : Actuation methods and mechanisms, Coord. Chem. Rev. 320–321 (2016) 38–52. doi:10.1016/j.ccr.2016.03.007.

[11] A. Belmonte, C. Russo, V. Ambrogi, X. Fernández-Francos, S. De la Flor, Epoxy-based shape-memory actuators obtained via dual-curing of off-stoichiometric “thiol-epoxy” mixtures, Polymers. 9 (2017) 113. doi:10.3390/polym9030113.

[12] J. Leng, K. Yu, J. Sun, Y. Liu, Deployable morphing structure based on shape memory polymer, Aircr. Eng. Aerosp. Technol. 87 (2015) 218–223. doi:10.1108/AEAT-06-2013-0118.

[13] J.J. Song, H.H. Chang, H.E. Naguib, Biocompatible shape memory polymer actuators with high force capabilities, Eur. Polym. J. 67 (2015) 186–198. doi:10.1016/j.eurpolymj.2015.03.067.

[14] Y. Li, C. Pruitt, O. Rios, L. Wei, M. Rock, J.K. Keum, A.G. Mcdonald, M.R. Kessler, Controlled shape memory behavior of a smectic main-chain liquid crystalline elastomer, Macromolecules. 48 (2015) 2864–2874. doi:10.1021/acs.macromol.5b00519.

[15] G.C. Lama, P. Cerruti, M. Lavorgna, C. Carfagna, V. Ambrogi, G. Gentile, Controlled Actuation of a Carbon Nanotube/Epoxy Shape-Memory Liquid Crystalline Elastomer, J. Phys. Chem. C. 120 (2016) 24417–24426. doi:10.1021/acs.jpcc.6b06550.

[16] M. Giamberini, P. Cerruti, V. Ambrogi, C. Vestito, F. Covino, C. Carfagna, Liquid crystalline elastomers based on diglycidyl terminated rigid monomers and aliphatic acids. Part 2. Mechanical characterization, Polymer. 46 (2005) 9113–9125. doi:10.1016/j.polymer.2005.04.093.

[17] B.A. Kowalski, T.C. Guin, A.D. Auguste, N.P. Godman, T.J. White, Pixelated Polymers: Directed Self Assembly of Liquid Crystalline Polymer Networks, ACS Macro Lett. 6 (2017) 436–441. doi:10.1021/acsmacrolett.7b00116.

[18] C. Ohm, M. Brehmer, R. Zentel, Liquid crystalline elastomers as actuators and sensors., Adv. Mater. 22 (2010) 3366–3387. doi:10.1002/adma.200904059.

[19] H. Yang, G. Ye, X. Wang, P. Keller, Micron-sized liquid crystalline elastomer actuators, Soft Matter. 7 (2011) 815–823. doi:10.1039/C0SM00734J.

[20] T.J. White, D.J. Broer, Programmable and adaptive mechanics with liquid crystal polymer networks and elastomers, Nat. Mater. 14 (2015) 1087–1098. doi:10.1038/nmat4433.

[21] J. Zhou, S.A. Turner, S.M. Brosnan, Q. Li, J.M.Y. Carrillo, D. Nykypanchuk, O. Gang, V.S. Ashby, A. V. Dobrynin, S.S. Sheiko, Shapeshifting: Reversible shape memory in semicrystalline elastomers, Macromolecules. 47 (2014) 1768–1776. doi:10.1021/ma4023185.

[22] Y. Meng, J. Jiang, M. Anthamattern, Shape actuation via internal stress-induced crystallization of dual-cure networks, ACS Macro Lett. 4 (2015) 115–118.

[23] M. Behl, K. Kratz, U. Noechel, T. Sauter, A. Lendlein, Temperature-memory polymer actuators,

Proc. Natl. Acad. Sci. 110 (2013) 12555–12559. doi:10.1073/pnas.1301895110.

[24] M. Behl, K. Kratz, J. Zotzmann, U. Nöchel, A. Lendlein, Reversible bidirectional shape-memory polymers, Adv. Mater. 25 (2013) 4466–4469. doi:10.1002/adma.201300880.

[25] J. Zhou, S.S. Sheiko, Reversible shape-shifting in polymeric materials, J. Polym. Sci. Part B Polym. Phys. 1 (2016) 1–16. doi:10.1002/polb.24014.

[26] C.L. Lewis, E.M. Dell, A Review of Shape Memory Polymers Bearing Reversible Binding Groups, J. Polym. Sci. Part B Polym. Phys. 54 (2016) 1340–1364. doi:10.1002/polb.23994.

[27] K.K. Westbrook, P.T. Mather, V. Parakh, M.L. Dunn, Q. Ge, B.M. Lee, H.J. Qi, Two-way reversible shape memory effects in a free-standing polymer composite, Smart Mater. Struct. 20 (2011) 65010. doi:10.1088/0964-1726/20/6/065010.

[28] Q. Ge, K.K. Westbrook, P.T. Mather, M.L. Dunn, H. Jerry Qi, Thermomechanical behavior of a two-way shape memory composite actuator, Smart Mater. Struct. 22 (2013) 55009. doi:10.1088/0964-1726/22/5/055009.

[29] M.O. Saed, A.H. Torbati, C.A. Starr, R. Visvanathan, N.A. Clark, C.M. Yakacki, Thiol-Acrylate Main-Chain Liquid-Crystalline Elastomers with Tunable Thermomechanical Properties and Actuation Strain, J. Polym. Sci. Part B Polym. Phys. 55 (2017) 157-168. doi:10.1002/polb.24249.

[30] M.O. Saed, A.H. Torbati, D.P. Nair, C.M. Yakacki, Synthesis of Programmable Main-chain Liquid-crystalline Elastomers Using a Two-stage Thiol-acrylate Reaction, J. Vis. Exp. 107 (2016) 1–10. doi:10.3791/53546.

[31] E. Zharinova, M. Heuchel, T. Weigel, D. Gerber, K. Kratz, Water-blown polyurethane foams showing a reversible shape-memory effect, Polymers. 8 (2016) 412.

[32] X. Fernández-Francos, A.-O. Konuray, A. Belmonte, S. De la Flor, À. Serra, X. Ramis, Sequential curing of off-stoichiometric thiol–epoxy thermosets with a custom-tailored structure, Polym. Chem. 7 (2016) 2280–2290. doi:10.1039/C6PY00099A.

[33] A. Belmonte, L. Giuseppe C., G. Gentile, P. Cerruti, V. Ambrogi, X. Fernández-Francos, S. De la Flor, Synthesis and characterization of liquid-crystalline elastomers: towards autonomous shape-memory actuation, J. Phys. Chem. C. (2017) (in press).

[34] A. Belmonte, X. Fernández-Francos, À. Serra, S. De la Flor, Phenomenological characterization of sequential dual-curing of off-stoichiometric " thiol-epoxy " systems : Towards applicability, Mater. Des. 113 (2017) 116–127. doi:10.1016/j.matdes.2016.10.009.

[35] J.-P. Pascault, H. Sautereau, V. J, W.J.J. R, Thermosetting Polymers, CRC Press, 2002.

[36] M. Giamberini, E. Amendola, C. Carfagna, Liquid Crystalline Epoxy Thermosets, Mol. Cryst. Liq. Cryst. Sci. Technol. Sect. A. Mol. Cryst. Liq. Cryst. 266 (1995) 9–22.

[37] C.-H. Hsueh, Modeling of elastic deformation of multilayers due to residual stresses and external bending, J. Appl. Phys. 91 (2002) 9652–9656.

[38] J. Malzbender, Mechanical and thermal stresses in multilayered materials, J. Appl. Phys. 95 (2004) 1780–1782. doi:10.1063/1.1642289.

[39] A. Pizzi, Principles of Polymer Networking and Gel Theory in Thermosetting Adhesive Formulations, Taylor & Francis Group, 2003.

[40] T.H. Ware, J.S. Biggins, A.F. Shick, M. Warner, T.J. White, Localized soft elasticity in liquid crystal elastomers., Nat. Commun. 7 (2016) 10781. doi:10.1038/ncomms10781.

[41] M. Shimbo, M. Ochi, Y. Shigeta, Srinkage and internal stress during curing of epoxide resins, J. Appl. Polym. Sci. 26 (1981) 2265–2277. doi:10.1002/app.1981.070260714.

[42] J.F. Ban, S.R. Lu, D. Guo, K. Liu, C.X. Luo, Thermomechanical Properties and Morphology of Liquid Crystalline Polyurethane/Epoxy Resin Composites, Adv. Mater. Res. 194–196 (2011) 1421–1425. doi:10.4028/www.scientific.net/AMR.194-196.1421.